Am J Transl Res 2023;15(3):1704-1714
www.ajtr.org /ISSN:1943-8141/AJTR0147613

Original Article

Carbon nanotube stimulation of human mononuclear cells to model granulomatous inflammation

Mrinalini Kala[1], Nancy G Casanova[2], Anlin Feng[3], Jeffrey R Jacobsen[4], Garrett Grischo[1], Ying Liang[3], Yesenia Moreno[1], Ting Wang[1,3], Kenneth S Knox[1]

[1]Department of Internal Medicine, University of Arizona College of Medicine Phoenix, Phoenix, AZ, United States; [2]Department of Medicine, University of Arizona, Tucson, AZ, United States; [3]Center for Translational Science, Florida International University, Port Saint Lucie, FL, United States; [4]Department of Pathology, University of Utah School of Medicine and ARUP Lab, United States

Received November 8, 2022; Accepted February 6, 2023; Epub March 15, 2023; Published March 30, 2023

Abstract: Objectives: Sarcoidosis is a multisystem inflammatory granulomatous disease of unknown etiology. The disease most often affects the lung and leads to death in 5% of patients. Patients who die often succumb due to progressive fibrotic lung disease. Translational research in sarcoidosis is significantly limited by a paucity of available experimental models. Carbon nanotubes are released into the environment during fuel combustion, manufacturing, and natural fires. Exposed individuals are at risk for cancer, lung inflammation and other chronic pulmonary disorders, including diseases resembling sarcoidosis and pulmonary fibrosis. In this study, we developed and characterized an *in vitro* experimental model relevant to sarcoidosis using human peripheral blood mononuclear cells (PBMCs) exposed to multiwalled carbon nanotubes (MWCNTs). Methods: MWCNT-exposed PBMCs were cultured and analyzed by Giemsa staining, immunohistochemistry (IHC) and RNA-seq analysis on days 1 and 7. Normalization and differential expression were calculated using DESeq2, Limma and edgeR methods from Bioconductor (adjP, log2Fold change and rawP). Results: MWCNT stimulation of PBMCs from healthy subjects leads to the formation of granuloma-like cell clusters and stereotypical inflammatory cytokine secretion. PBMC transcriptomic analysis demonstrated activation of defense- and inflammation-related pathways, including the Jak-Stat pathway and TNF signaling pathway. Conclusions: This model is unique, as cell clustering is seen in the absence of specific antigenic stimulation (e.g., mycobacterial) or the addition of exogenous cytokines. Modeling with PBMCs provides a platform for precision medicine and evaluation of future therapies for granulomatous and fibrotic lung diseases.

Keywords: Granuloma, sarcoidosis, *in vitro* model, MWCNTs, PBMCs, cytokines, gene expression

Introduction

Granulomatous inflammation typically manifests as a protective immune response to mycobacterial and fungal infections. The cellular characteristics of granulomas, histologically, are well defined and involve activated macrophages and reticuloendothelial cells surrounded by T cells. This orchestrated inflammatory response, however, can also be seen in foreign body reactions and in response to noninfectious stimuli such as exposure to hard metals and silica [1, 2]. Granulomatous inflammation is the hallmark of berylliosis, sarcoidosis and hypersensitivity pneumonitis [1, 3]. Granulomatous processes may persist and can last for years, leading to tissue destruction and fibrosis [3]. Occupational health data and animal studies have shown that carbon nanotube exposure can lead to granulomatous diseases resembling sarcoidosis [4-6].

Sarcoidosis is a complex granulomatous lung disease of unknown cause [4]. The incidence ranges from 5 to 40 cases per 100,000 people. Progress in research for diseases such as sarcoidosis is slow owing to our inability to identify an etiologic agent and a paucity of experimental models that recapitulate the complexities of human disease. *In vitro* models using peripheral blood mononuclear cells (PBMCs) have emerged as a tool to study human immune responses to infectious and noninfectious granulomagenic stimuli [7-10]. Obtaining PBMCs

from patients is relatively straightforward and shows promise for more personalized platforms.

Carbon nanotubes (CNTs) are allotropes of carbon generally classified into three types: single-walled carbon nanotubes (SWCNTs), multiwalled carbon nanotubes (MWCNTs, outer diameter < 15 nm) and carbon nanofibers (CNFs, outer diameter above 15 nm). MWCNTs are a stack of graphene sheets rolled up into concentric cylinders. Each nanotube is a single molecule with diameters as small as 0.7 nm. CNTs are distinct from CNFs, which are not single molecules but strands of layered-graphite sheets [11]. CNTs are used in a wide variety of applications: medical devices, drug delivery, imaging, air water filtration, ceramics, solar collection, and fabrics [12]. Carbon nanotubes are also released into the environment from fuel combustion, manufacturing, and natural fires and are associated with pulmonary morbidity [4-8]. *In vivo* studies of CNTs in animal models have shown granulomatous and fibrotic pulmonary manifestations [5, 6, 9-15]. One important epidemiological report detailed that many first responders of the World Trade Center tragedy developed pulmonary diseases, including sarcoidosis. A unifying theme is that their lung biopsies showed the presence of carbon nanotubes [14].

Published *in vitro* models of sarcoidosis stimulate donor PBMCs with mycobacterial antigens [8, 9]. To our knowledge, a human *in vitro* model that uses noninfectious exposures to stimulate granuloma-like inflammation does not exist. In this study, we used MWCNTs to induce granuloma-like inflammation *in vitro* in PBMCs from healthy volunteers as a first step toward developing a personalized model for those with relevant diseases. Gene expression of immune clusters revealed pathways common to those described for sarcoidosis and related inflammatory diseases. Occupational health data [4, 13, 14] and animal studies [15, 16] indicate that this model could be highly relevant in the study of granulomatous or fibrotic diseases.

Materials and methods

Human blood samples

After obtaining informed consent (University of Arizona IRB approval #1907775403), 50 cc blood was collected by standard venipuncture from healthy donors. Blood was collected into heparinized tubes and processed within 2 hours to store PBMCs.

Isolation and culture of human PBMCs

Human PBMCs were isolated from whole blood using Ficoll-Paque plus reagent (GE Healthcare Biosciences, Piscataway, NJ) and cryopreserved in liquid nitrogen. Thawed PBMCs were washed and reconstituted in complete RPMI culture media (Fisher Scientific, Hampton, NH) and cultured in 96-well plates (3.5×10^5 cells/well) coated with collagen, Matrigel, or agarose. Cell viability was assessed on days 4, 7, 10, and 14 using the CellTiter-Glo 3D cell viability assay (Promega, Madison, WI).

Sublethal dose determination of MWCNTs

MWCNT reagent was acquired from Nanoshel (Wilmington, DE) to stimulate PBMCs. PBMCs were cultured at 3.5×10^5 cells/well on collagen-coated 96-well plates and treated with 0, 0.5, 1, 5, or 10 μg/ml/cm^2 MWCNTs. The cells were assessed for viability on days 4, 7, 10 and 14 by using the CellTiter-Glo 3D cell viability assay (Promega, Madison, WI) following the manufacturer's instructions.

PBMC stimulation with MWCNTs

PBMCs were plated at 3.5×10^5 PBMCs/well on collagen-coated glass chambered slides (Cell Treat, Pepperell, MA). Cells were exposed to 0.25 μg/ml MWCNTs for 20 minutes, and medium was added to a final volume of 700 μl. Cells were cultured and harvested on days 1 and 7 by gentle pipetting and Cytospin at 500 rpm for 5 min.

Giemsa staining

Cytospin cells were stained with May-Grünwald-Giemsa (Thermo Fisher Scientific, Waltham, MA) to confirm the granuloma-like immune cell clusters. The slides were air dried for 30-40 min at RT, and Giemsa staining was performed using the Siemens Hematek 3000 slide stainer with an Epredia-Richard-Allan scientific modified Wright stain pack (Thermo Fisher Scientific, Waltham, MA). Slides were air dried and mounted using the Sekura Tissue-Tek Film automated coverslipper. Light micrographs

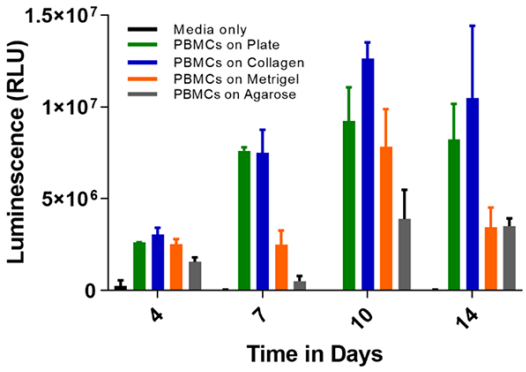

Figure 1. Time-dependent PBMC viability with different coating matrices. PBMCs were cultured on plates with different coating matrices for 14 days, and cell numbers were measured by luminescence (CellTiter Glo, Promega). The collagen-coated surface provided enhanced growth and viability to PBMCs compared to Matrigel and agarose. Bar represents the mean ± SD.

were taken using an Olympus BX53 microscope, a Lumenera Le575 camera (Olympus, San Jose, CA) and ECHO revolve R4 microscope (ECHO, San Diego, CA) for cluster morphology.

Measuring the size and area of granuloma-like cell clusters

The size and area of the granuloma-like clusters were determined semiquantitatively on day 7 by microscopy. We used the software tool from ECHO revolve R4 microscope (San Diego, CA) to determine the area and size of the clusters.

IHC staining

CD3 (LN10-Leica) and CD68 (514H12-Leica) staining was performed using heat-induced epitope retrieval for 20 minutes with ER2 on the Leica Bond platform at pH 8.9-9.1. Slides were air dried and mounted using the Sekura Tissue-Tek Film automated coverslipper. Light micrographs were taken using an Olympus BX53 microscope and a Lumenera Le575 camera (Olympus, San Jose, CA).

Transmission electron microscopy

PBMCs treated with MWCNTs were fixed and processed according to conventional transmission electron microscopy (TEM) procedures using chemical fixation. Briefly, samples were treated sequentially with buffered 2% glutaraldehyde and 1% osmium tetroxide and then stained with 2% aqueous uranyl acetate. This step was followed by dehydration in a graded ethanol series and transition to anhydrous propylene oxide. Cells were then infiltrated and ultimately embedded in the standard mixture of Spurr's epoxy resin described by Ellis [17]. Polymerized blocks were ultrathin sectioned at 70 nm thickness using a Leica Ultracut-R microtome, and the sections were collected on formvar-coated copper slot grids. Poststaining was performed using 2% uranyl acetate in 50% ethanol and Sato's lead citrate [18]. Images were generated and acquired using a Philips CM200 FE-TEM operated at 200 kV.

Cytokine analysis

Supernatants collected from MWCNT-treated and untreated PBMCs on day 7 were analyzed for GM-CSF, IFN-γ, IL-1β, IL-2, IL-4, IL-5, IL-6, IL-7, IL-8, IL-10, IL-12 (p70), IL-13, and TNF-α using the 13 plex MILLIPLEX® MAP Human High Sensitivity T-Cell Magnetic Bead Panel (Millipore Sigma, Burlington, MA). The data were analyzed using Belysa immunoassay curve fitting software (Millipore Sigma, Burlington, MA).

Statistical analysis

Data were analyzed using GraphPad software (GraphPad, Inc., CA). All results are presented as the mean ± standard deviation (SD). Differences were compared using Student's t test or analysis of variance (ANOVA). A p value < 0.05 was considered statistically significant. The results of the number and area of granuloma-like clusters were compared between untreated and MWCNT-treated PBMCs with ANOVA. The results of differences in the cytokine profile were compared between untreated and MWCNT-treated PBMCs with a paired t test.

Gene expression analysis of PBMCs stimulated with MWCNTs

We conducted ribonucleic acid (RNA) sequencing in PBMCs from healthy subjects stimulated with MWCNTs (0.25 μg/ml) and assessed the transcriptome changes compared to those of untreated PBMCs. PBMCs were harvested on day 1 and day 7. Total RNA was purified, and DNase treated using the Qiagen RNA purification kit (Redwood City, CA) according to the

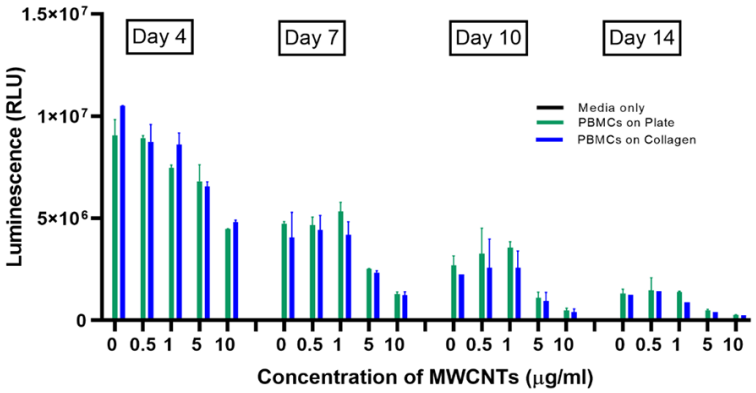

Figure 2. Time- and dose-dependent effects of MWCNTs on PBMC viability. PBMCs were cultured with MWCNTs (0-10 μg/mL) for 14 days, and cell numbers were measured by luminescence (CellTiter Glo, Promega). MWCNTs inhibit PBMC viability in a time- and dose-dependent manner. Bar represents the mean ± SD.

manufacturer's protocol. RNA integrity was evaluated using the RNA Nano 6000 Assay Kit of the Bioanalyzer 2100 system (Agilent Technologies, CA). Library preparation was performed, and clustering generation sequencing was conducted using Illumina HiSeq 3000 (Novagene, Sacramento, CA). RNAseq raw data processing was conducted using HISAT2 (Hierarchical Indexing for Spliced Alignments of Transcripts) [19] and Bowtie2 [20] to align and clean reads to the reference genome and the reference genes [21]. The abundance and distribution of transcripts were assessed by obtaining an expected number of fragments per kilobase of transcript per million mapped reads (FPKM). Correlation analysis to assess variation between samples was performed by Pearson correlation. We conducted between-sample normalization using the trimmed mean of M-values.

Differential expression analysis

Normalization and differential expression were calculated using DESeq2, Limma and edgeR packages from Bioconductor [22]. To control for multiple testing error, we used the adjusted *P* value false discovery rate (FDR) as our adjusted *P* value [23]. Transcript dysregulation was deemed statistically significant if the false discovery rate (FDR) was < 0.05 and fold change (FC) > 1.5 within transcript contrasts. Assessment of the overrepresentation of identified differentially expressed genes (DEGs) in each group was determined using enrichment analysis. Gene Ontology (GO) [24] classification was focused on biological process and pathway classification with KEGG and Reactome [25, 26]. Protein association networks were calculated on the DEGs with STRING (v. 11) [27]. Gene set enrichment analysis (GSEA) was conducted to calculate the presence of enrichment against previously defined sets of genes in biological pathways [28, 29], and FDR < 0.10 was set as the cut off level of significance.

Results

PBMC viability

PBMCs were cultured over 14 days on 96-well plates coated with collagen, Matrigel, or agarose. The PBMC viability was measured using the CellTiter-Glo 3D cell assay. PBMC growth and cell viability were higher on uncoated and collagen-coated plates compared to those of cells growing on Matrigel- or agarose-coated plates (**Figure 1**). Low doses of MWCNTs showed better viability/growth (**Figure 2**). Based on these data, we chose to culture PBMCs for 7 days after MWCNT exposure for all *in vitro* characterization experiments.

In vitro granuloma-like clusters

Compared to unstimulated PBMCs (**Figure 3A**), MWCNT-challenged PBMCs (**Figure 3B**) (0.25 μg/ml, 7 days) exhibited organized clusters of highly vacuolated macrophages rosetted by T cells. The number of clusters was significantly higher for the 0.25 μg/ml MWCNT-treated PBMCs than that for the untreated control cells and cells with a lower dose (0.05 μg/ml) of MWCNTs (**Figure 3C**). The cluster area was significantly larger for the PBMCs treated with 0.05 and 0.25 μg/ml of MWCNTs than that for the untreated controls (**Figure 3D**). Giemsa staining showed that these granuloma-like clusters were sustainable in culture beyond day 10 (data not shown). Similarly, CD68 (intracellular macrophage marker, yellow) and CD3 (surface T-cell marker, red) IHC staining of the PBMCs treated with 0.25 μg/ml of MWCNTs after day 7 showed large organized clusters of highly vacuolated macrophages surrounded by T cells (**Figure 3E** and **3F**).

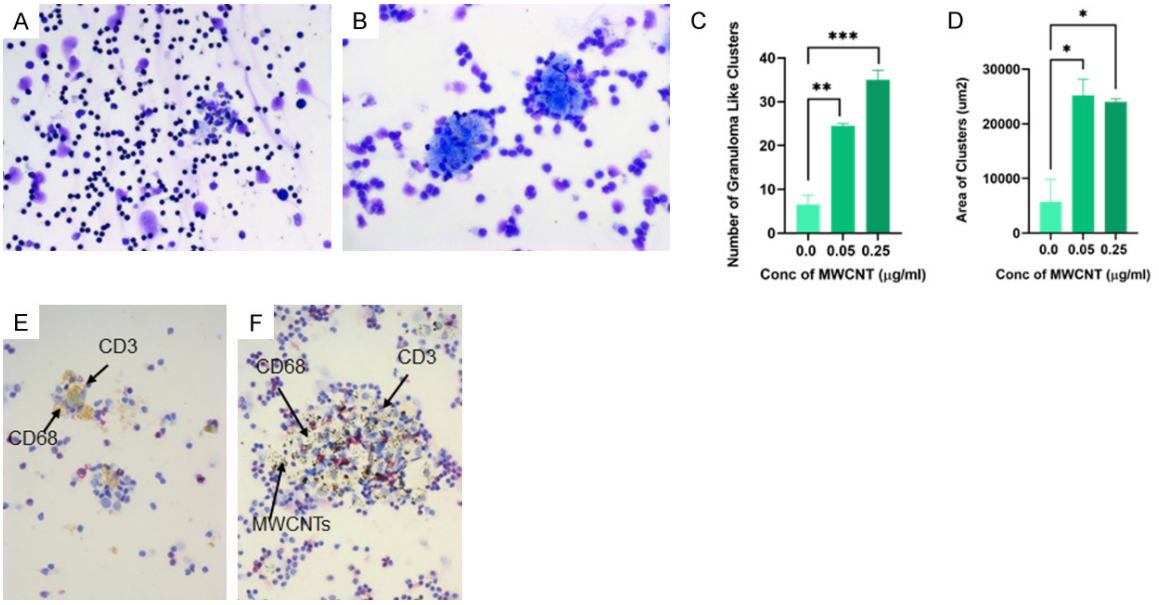

Figure 3. MWCNT stimulation induced granuloma-like clusters. PBMCs were cultured with (A) no MWCNTs and (B) 0.25 μg/mL MWCNTs for 7 days. Giemsa staining was performed to analyze the morphology of granuloma-like cell clusters. (C) The total number and (D) size of *in vitro* granuloma-like clusters were measured using standard microscopy software. MWCNTs exposure significantly increased the total number and size of granuloma-like clusters. *P < 0.05, **P=0.00481, ***P=0.001. These cultured PBMCs were also stained with 3' diaminobenzidine (CD68, a macrophage marker, light brown staining) and 3-amino-9-ethylcarbazole (CD3, T-cell marker, red staining). (E) Untreated PBMCs stained for CD68 and CD3 after 7 days of culture show loosely aggregated cells commonly seen in cell culture. (F) CD68 and CD3 staining of PBMCs treated with 0.25 μg/mL MWCNTs after 7 days of culture. Large organized clusters of highly vacuolated macrophages are surrounded by T cells, resembling granulomas. MWCNTs are noted (black dots) inside macrophages.

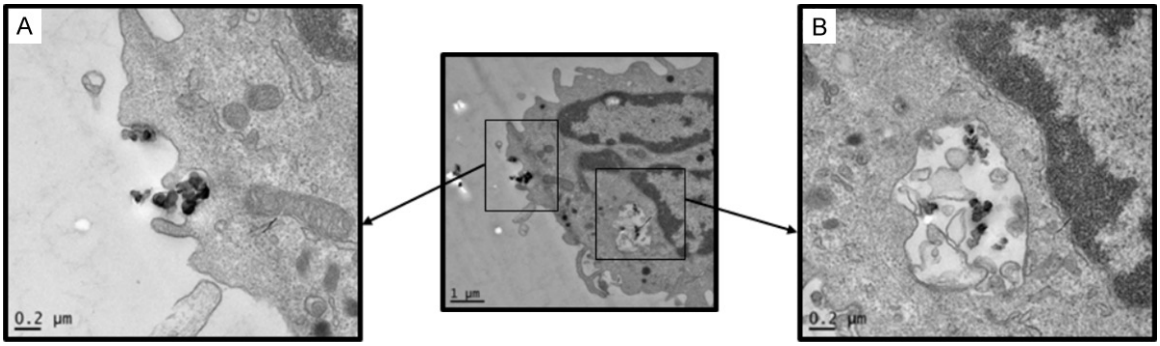

Figure 4. Transmission electron microscopy (TEM) image of MWCNT uptake by a macrophage. A. Shows an invagination of the cell membrane with a collection of MWCNTs in the process of being engulfed by the cell. B. MWCNTs contained within a distinct cellular vesicle.

Transmission electron microscopy

Transmission electron microscopy showed uptake of MWCNTs by PBMCs (**Figure 4**). **Figure 4A** shows MWCNTs aggregating around an invaginated cell membrane. The boxed TEM image shows that MWCNTs were engulfed by membrane invagination and enclosed within a cellular vesicle characterized morphologically as a vacuole (**Figure 4B**).

Cytokine profiles

There was a significant increase in PBMC secretion of the proinflammatory cytokines TNFα, IL-6, and IL-10 in response to MWCNTs

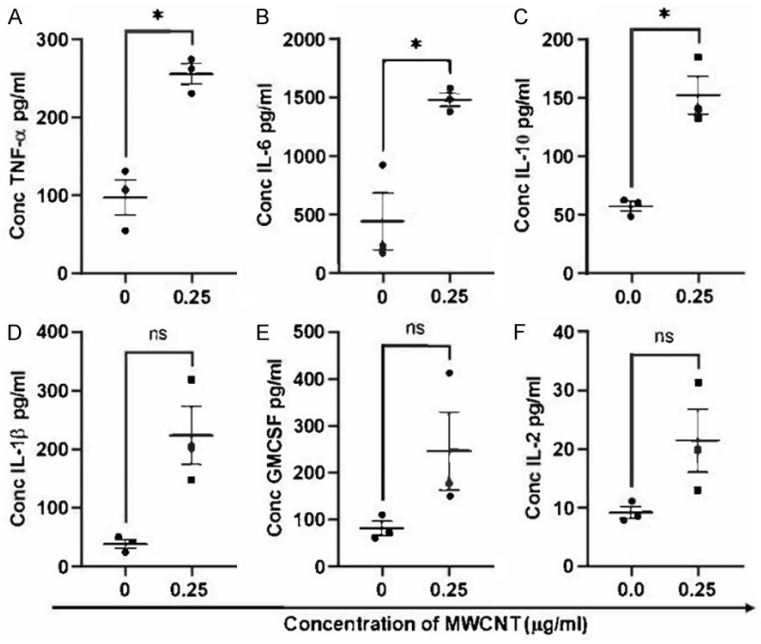

Figure 5. MWCNT stimulation induced proinflammatory cytokine release from PBMCs. Human PBMCs were challenged with 0.25 μg/mL MWCNTs and cultured for 7 days. A human T-cell 13-plex cytokine assay was performed on collected culture media. The cytokines TNFα, IL-6, and IL-10 exhibited significant increases in treated cells compared to controls (*P=0.025, *P=0.034, *P=0.022, respectively). The cytokines IL-2, IL-1β, and GM-CSF displayed an increasing trend in treated PBMCs compared to controls.

compared to that of the untreated controls on day 7 (**Figure 5A**: *P=0.025, **Figure 5B**: *P=0.034, **Figure 5C**: *P=0.022, respectively). Other proinflammatory cytokines, IL-2, IL-1β, and GM-CSF, were also increased (**Figure 5D-F**).

Gene expression

We analyzed the gene expression associated with MWCNT stimulation against unstimulated (controls) on day 1 and day 7. A total of 312 DEGs were identified in the MWCNT-stimulated PBMCs (FDR < 0.05, FC 1.5) on day 1, with 176 downregulated and 136 upregulated genes (**Figure 6A**). Two hundred of these DEGs were identified as protein-coding genes, which were significantly enriched for inflammation-related pathways (KEGG), such as leukocyte migration, cell motility, chemotaxis and migration, and defense response (**Figure 6B**). The total number of DEGs for day 7 was 802, with 411 downregulated and 390 upregulated genes (**Figure 6C**). The protein network interactions of these DEGs were analyzed. On day 1, we observed only 9 significantly enriched clusters, most significant within the immunoglobulin binding alpha-1B-glycoprotein/leukocyte immunoglobulin-like receptor. The interactome on day 7 identified clusters; a portion of these hierarchical subsets is shown in Supplementary Figure 1. Among the clusters, we identified the NF-kappa B signaling pathway, TIR domain (TNFRSF1A, TNFRSF14, TLR4, TLR5), proteins with immunoregulatory interactions (LILRB2, LILRB5, CD180, TLR2, CD14), and chemokine receptors that bind chemokines (CXCL3, CXCL5, CXCL10, CXCL11, CXCL9). A complete list of the protein clusters with the matching proteins is listed in Supplementary Table 1. The enrichment analysis for pathways indicated changes in the inflammatory response that involved dysregulation in genes within the ribosomal and lysosomal response, TNF signaling, and B and T-cell signaling (**Figure 6D**). The Gene Ontology (GO) for biological terms (FDR < 0.035) of the DEGs for both time points was analyzed separately; the downregulated genes were enriched in the terms for regulation of TNF, cytokine production, immune and inflammatory responses, while the upregulated gene set was associated with GO biological processes within the MAPK cascade, IL-1 response and ERK1 and ERK2 cascades. On day 7, the GO for biological processes yielded over 200 terms, the top ones associated with a downregulation of the inflammatory response and upregulated cellular processes involved in cell cycle regulation (Supplementary Figure 2).

Next, we conducted a gene set enrichment analysis (GSEA) targeting the JAK-STAT signaling pathway and TNF signaling pathways (KEGG) (**Figure 7**). Our results revealed that MWCNT stimulation caused a significant negative enrichment (NES -1.3, FDR 0.071) for JAK-STAT (**Figure 7A**) on day 1; this enrichment was not significant for the TNF signaling pathway (NES -0.75, FDR 0.38) (**Figure 7B**). The same analysis on day 7 revealed the opposite; JAK-

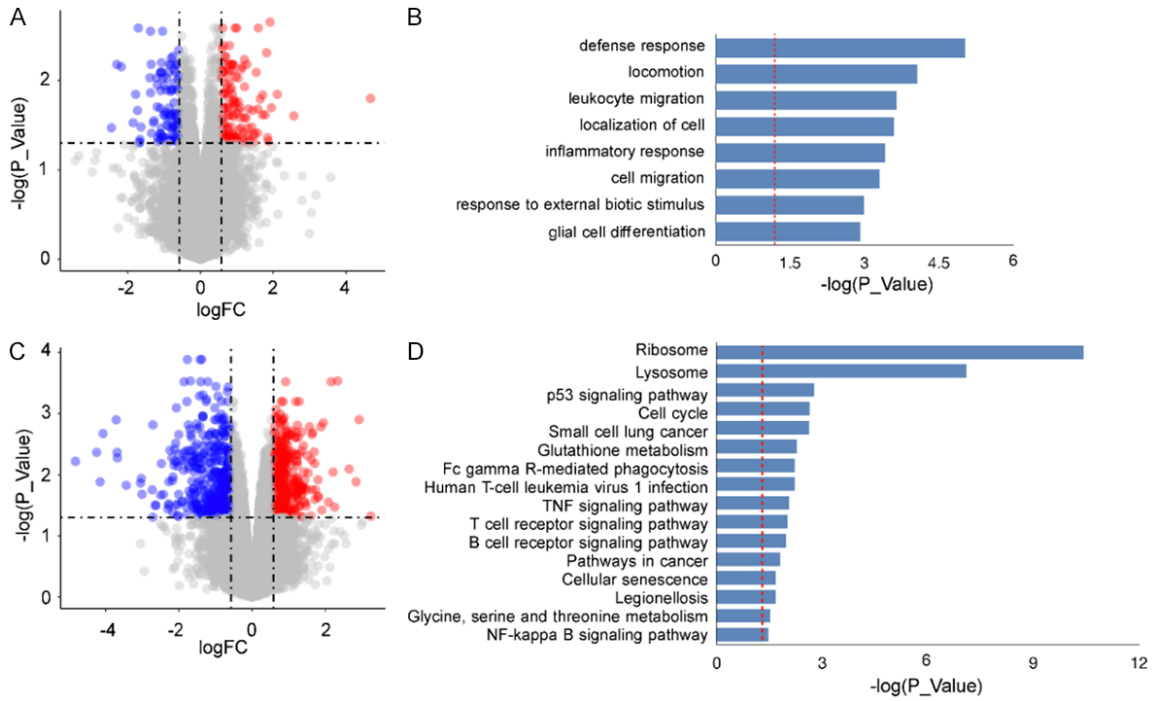

Figure 6. MWCNT-induced differential gene expression at day 1 (A and B) and day 7 (C and D). (A) Volcano plot showing the 312 differentially expressed genes (DEGs) comparing with PBMCs-MWCNT treated on day 1, with cutoffs of ±1.5 fold change (FC) and an adjusted *P* value < 0.05. Downregulated genes are shown in blue and upregulated in red. (B) KEGG pathways show the top pathways associated with the DEGs. (C) Volcano plot showing the 802 differentially expressed genes (DEGs) comparing with PBMCs-MWCNT treated on day 7, with cutoffs of ±1.5 fold change (FC) and an adjusted *P* value < 0.05. Downregulated genes are shown in blue and upregulated in red. (D) KEGG pathways dysregulated by MWCNTs at day 7.

STAT signaling enrichment was not significant (NES 0.96, FDR 0.3) (**Figure 7C**), while the TNF signaling pathway showed a significant positive enrichment (NES 1.29, FDR 0.09) (**Figure 7D**).

Discussion

The *in vitro* granuloma model described in this study is derived from healthy human PBMCs exposed to a noninfectious stimulus, MWCNTs. Utilizing a stimulus that is not infectious or antigenic is a unique aspect of this approach and is independent from any prior memory T-cell response. The proposed model recapitulates many features seen in bronchoalveolar lavage cytologic samples [30] and tissue granulomas of patients with sarcoidosis and granulomatous infections. These findings include granuloma-like cell clusters morphologically, enhanced proinflammatory cytokine production, and induction of gene expression pathways commonly dysregulated in inflammatory and granulomatous lung diseases. Current existing *in vitro* granuloma models are generated from PBMCs using mycobacterial antigens [7, 10] or Sepharose beads coated with PPD [8, 9]. These models were only able to generate immune clustering from PBMCs of individuals with sarcoidosis or a history of TB infection. While inherently valuable to discern disease from healthy individuals, our granuloma model is novel and generates granuloma-like clusters from PBMCs of healthy individuals, thereby making it feasible to use as a platform for studying disease mechanisms and treatment options. The significant increase in inflammatory cytokine secretion characteristic of this model (**Figure 5**) closely represents the inflammatory process that occurs in granulomatous diseases.

Our MWCNT model generated dysregulation of genes associated with an inflammatory response, which evolved over 7 days. A higher number of DEGs (802) on day 7, compared to the gene expression observed on day 1 (226 DEGs), was observed with dysregulation of pathways primarily associated with defense

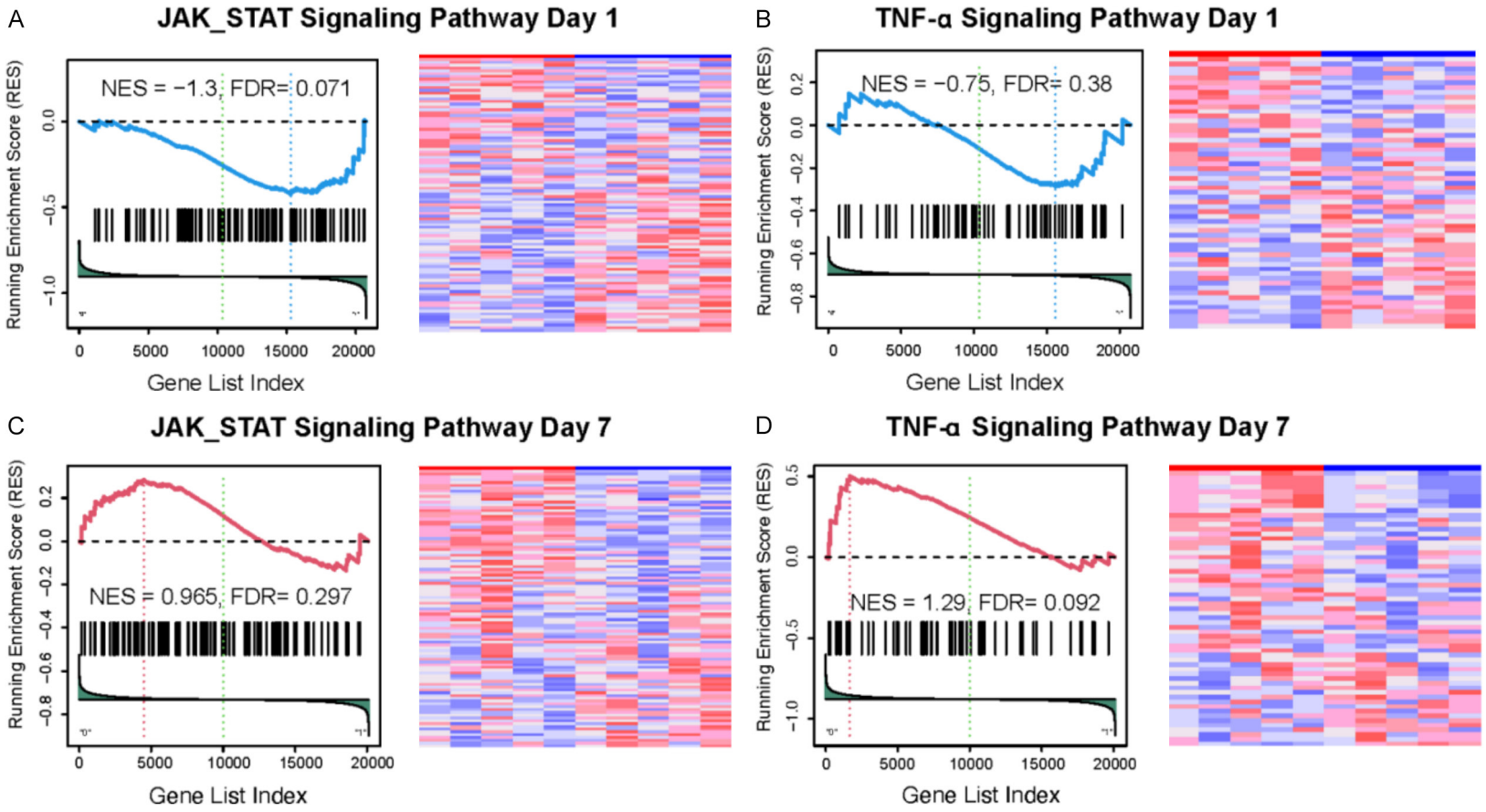

Figure 7. Gene set enrichment analysis (GSEA) targeting the JAK_STAT and TNF signaling pathways. MWCNT stimulation caused a significant negative enrichment (NES -1.3, FDR 0.07) for JAK-STAT (A) on day 1; the negative enrichment for TNF signaling pathway was not significant (NES -0.75, FDR 0.38). (B) The same pathways were positively enriched on day 7, JAK_STAT enrichment was not significant (NES 0.96, FDR 0.3) (C) but a significant positive enrichment for TNF signaling pathway (NES 1.29, FDR 0.92) was present. (D) The expression dataset sorted by correlation with phenotype, the corresponding heatmap, given a KEGG a priori set. The enrichment score was calculated using the normalized enrichment score (NES), and then we adjusted for multiple hypothesis testing using the false discovery rate (FDR). The blue curve corresponds to day 1, and the red curve corresponds to day 7.

response, cell migration, motility and chemotaxis on day 1. We observed that this gene expression was modified at seven days, showing intense ribosomal- and lysosomal-related activity, with dysregulation of T and B-cell receptor signaling. On day 7, the protein-protein interaction network showed interconnected clusters such as chemokine receptors, NF-kappa B singling and T receptor domain (TNFRS1A, CD14, TNFSF13, TLR5, TLR4). Soluble CD14 has been postulated as one marker of sarcoidosis activity [31].

Gene set enrichment analysis targeted the TNF signaling and JAK-STAT signaling pathways, both of which are prominently reported as key in granuloma development and maintenance, independent of whether the cause was of infectious or noninfectious origin [32-38]. Our MWCNT model corroborated the dysregulation of these pathways. GSEA indicated a significant negative enrichment for JAK-STAT on day 1 and for the TNF signaling pathway on day 7.

The MWCNT *in vitro* human granuloma model offers a novel platform for evaluating disease mechanisms, personalized responses and early phase drug discovery for treating sarcoidosis and other human granulomatous diseases. MWCNTs have been shown in mouse models to induce granulomatous inflammation similar to sarcoidosis [3, 5, 6], enhancing the validity of our *in vitro* experimental findings. This model demonstrates key characteristic features of granulomas at the cellular, protein and molecular levels. The novelty and appeal of this model is that it eliminates immunologic memory that may be required to generate *in vitro* granulomas in other models.

The shortcomings of our model are similar to those of other existing cell culture models. Utilizing PBMCs is convenient but limits the responding cell populations to immune cells. Granulomas are complex structures that form in organs where an abundance of cell types, tissue scaffolding, and trafficking are orchestrated and cannot be replicated *in vitro* [39]. While our readouts were measured longitudinally and showed significant evolution of gene expression over time, the static points in time give us merely a glimpse into the nanotube-induced granuloma-like response.

Future work will characterize and compare our model in subjects with sarcoidosis and assess gene expression profiles. Perturbing the model with treatments known to be effective in sarcoidosis, such as anti-TNF antibodies, will allow us to further examine potential uses of the model. Further validation of the responses seen in our model is underway utilizing publicly available PBMC and disease-specific datasets.

Acknowledgements

This work was supported in part by Arizona Biomedical Research Commission grant ADH-S18-198849 (KSK) and NIH grants P01HL-146369 and P01HL146369 (TW). We thank the clinical research and the biobank team for subject consent and PBMC processing and storage. We also thank Dave Lowry at the ASU electron microscopy core for helping with TEM preparation, image acquisition and analysis.

Disclosure of conflict of interest

None.

Address correspondence to: Dr. Mrinalini Kala, Department of Internal Medicine, University of Arizona College of Medicine Phoenix, 475 N 5th Street, BSPB, Rm E511, Phoenix, AZ 85004, United States. Tel: 6028272251; E-mail: mkala13@arizona.edu

References

[1] Majno G and Joris I. Cells, tissues, and disease: principles of general pathology. USA: Oxford University Press; 2004.

[2] Mukhopadhyay S and Gal AA. Granulomatous lung disease: an approach to the differential diagnosis. Arch Pathol Lab Med 2010; 134: 667-690.

[3] Kunkel SL, Lukacs NW, Strieter RM and Chensue SW. Animal models of granulomatous inflammation. Semin Respir Infect 1998; 13: 221-228.

[4] Newman KL and Newman LS. Occupational causes of sarcoidosis. Curr Opin Allergy Clin Immunol 2012; 12: 145-150.

[5] Soliman E, Bhalla S, Elhassanny AEM, Malur A, Ogburn D, Leffler N, Malur AG and Thomassen MJ. Myeloid ABCG1 deficiency enhances apoptosis and initiates efferocytosis in bronchoalveolar lavage cells of murine multi-walled carbon nanotube-induced granuloma model. Int J Mol Sci 2021; 23: 47.

[6] Barna BP, Malur A and Thomassen MJ. Studies in a murine granuloma model of instilled car-

bon nanotubes: relevance to sarcoidosis. Int J Mol Sci 2021; 22: 3705.
[7] Broos CE, van Nimwegen M, Hoogsteden HC, Hendriks RW, Kool M and van den Blink B. Granuloma formation in pulmonary sarcoidosis. Front Immunol 2013; 4: 437.
[8] Crouser ED, White P, Caceres EG, Julian MW, Papp AC, Locke LW, Sadee W and Schlesinger LS. A novel in vitro human granuloma model of sarcoidosis and latent tuberculosis infection. Am J Respir Cell Mol Biol 2017; 57: 487-498.
[9] Kapoor N, Pawar S, Sirakova TD, Deb C, Warren WL and Kolattukudy PE. Human granuloma in vitro model, for TB dormancy and resuscitation. PLoS One 2013; 8: e53657.
[10] Wang H, Maeda Y, Fukutomi Y and Makino M. An in vitro model of Mycobacterium leprae induced granuloma formation. BMC Infect Dis 2013; 13: 279.
[11] Lin T, Bajpai V, Ji T and Dai L. Chemistry of carbon nanotubes. Aust J Chem 2003; 56: 635-651.
[12] Gao L, Grant A, Halder I, Brower R, Sevransky J, Maloney JP, Moss M, Shanholtz C, Yates CR, Meduri GU, Shriver MD, Ingersoll R, Scott AF, Beaty TH, Moitra J, Ma SF, Ye SQ, Barnes KC and Garcia JG. Novel polymorphisms in the myosin light chain kinase gene confer risk for acute lung injury. Am J Respir Cell Mol Biol 2006; 34: 487-495.
[13] Beard JD, Erdely A, Dahm MM, de Perio MA, Birch ME, Evans DE, Fernback JE, Eye T, Kodali V, Mercer RR, Bertke SJ and Schubauer-Berigan MK. Carbon nanotube and nanofiber exposure and sputum and blood biomarkers of early effect among U.S. workers. Environ Int 2018; 116: 214-228.
[14] Wu M, Gordon RE, Herbert R, Padilla M, Moline J, Mendelson D, Litle V, Travis WD and Gil J. Case report: lung disease in world trade center responders exposed to dust and smoke: carbon nanotubes found in the lungs of world trade center patients and dust samples. Environ Health Perspect 2010; 118: 499-504.
[15] Ray JL and Holian A. Sex differences in the inflammatory immune response to multi-walled carbon nanotubes and crystalline silica. Inhal Toxicol 2019; 31: 285-297.
[16] Shvedova AA, Yanamala N, Kisin ER, Tkach AV, Murray AR, Hubbs A, Chirila MM, Keohavong P, Sycheva LP, Kagan VE and Castranova V. Long-term effects of carbon containing engineered nanomaterials and asbestos in the lung: one year postexposure comparisons. Am J Physiol Lung Cell Mol Physiol 2014; 306: L170-L182.
[17] Ellis EA. Solutions to the problem of substitution of ERL 4221 for vinyl cyclohexene dioxide in spurr low viscosity embedding formulations. Microsc Today 2006; 14: 32-33.
[18] Hanaichi T, Sato T, Iwamoto T, Malavasi-Yamashiro J, Hoshino M and Mizuno N. A stable lead by modification of Sato's method. J Electron Microsc (Tokyo) 1986; 35: 304-306.
[19] Kim D, Langmead B and Salzberg SL. HISAT: a fast spliced aligner with low memory requirements. Nat Methods 2015; 12: 357-360.
[20] Langmead B and Salzberg SL. Fast gapped-read alignment with bowtie 2. Nat Methods 2012; 9: 357-359.
[21] Li B and Dewey CN. RSEM: accurate transcript quantification from RNA-Seq data with or without a reference genome. BMC Bioinformatics 2011; 12: 323.
[22] Gentleman RC, Carey VJ, Bates DM, Bolstad B, Dettling M, Dudoit S, Ellis B, Gautier L, Ge Y, Gentry J, Hornik K, Hothorn T, Huber W, Iacus S, Irizarry R, Leisch F, Li C, Maechler M, Rossini AJ, Sawitzki G, Smith C, Smyth G, Tierney L, Yang JY and Zhang J. Bioconductor: open software development for computational biology and bioinformatics. Genome Biol 2004; 5: R80.
[23] Benjamini Y and Hochberg Y. Controlling the false discovery rate: a practical and powerful approach to multiple testing. J R Stat Soc B (Methodol) 1995; 57: 289-300.
[24] Gene Ontology Consortium. Gene ontology consortium: going forward. Nucleic Acids Res 2015; 43: D1049-D1056.
[25] Fabregat A, Sidiropoulos K, Viteri G, Forner O, Marin-Garcia P, Arnau V, D'Eustachio P, Stein L and Hermjakob H. Reactome pathway analysis: a high-performance in-memory approach. BMC Bioinformatics 2017; 18: 142.
[26] Kanehisa M, Goto S, Kawashima S, Okuno Y and Hattori M. The KEGG resource for deciphering the genome. Nucleic Acids Res 2004; 32: D277-D280.
[27] Szklarczyk D, Gable AL, Lyon D, Junge A, Wyder S, Huerta-Cepas J, Simonovic M, Doncheva NT, Morris JH, Bork P, Jensen LJ and Mering CV. STRING v11: protein-protein association networks with increased coverage, supporting functional discovery in genome-wide experimental datasets. Nucleic Acids Res 2019; 47: D607-D613.
[28] Subramanian A, Tamayo P, Mootha VK, Mukherjee S, Ebert BL, Gillette MA, Paulovich A, Pomeroy SL, Golub TR, Lander ES and Mesirov JP. Gene set enrichment analysis: a knowledge-based approach for interpreting genome-wide expression profiles. Proc Natl Acad Sci U S A 2005; 102: 15545-15550.
[29] Wang X and Cairns MJ. SeqGSEA: a Bioconductor package for gene set enrichment analysis of RNA-Seq data integrating differential expression and splicing. Bioinformatics 2014; 30: 1777-1779.

[30] Smith PA, Kohli LM, Wood KL, Hage CA, Twigg HL and Knox KS. Cytometric analysis of BAL T cells labeled with a standardized antibody cocktail correlates with immunohistochemical staining. Cytometry B Clin Cytom 2006; 70: 170-178.

[31] Homolka J, Lorenz J, Zuchold HD and Muller-Quernheim J. Evaluation of soluble CD 14 and neopterin as serum parameters of the inflammatory activity of pulmonary sarcoidosis. Clin Investig 1992; 70: 909-916.

[32] Amber KT, Bloom R, Mrowietz U and Hertl M. TNF-alpha: a treatment target or cause of sarcoidosis? J Eur Acad Dermatol Venereol 2015; 29: 2104-2111.

[33] Casanova NG, Gonzalez-Garay ML, Sun B, Bime C, Sun X, Knox KS, Crouser ED, Sammani N, Gonzales T, Natt B, Chaudhary S, Lussier Y and Garcia JGN. Differential transcriptomics in sarcoidosis lung and lymph node granulomas with comparisons to pathogen-specific granulomas. Respir Res 2020; 21: 321.

[34] Christoforidou A, Goudakos J, Bobos M, Lefkaditis E, Vital V and Markou K. Sarcoidosis-like granulomatosis of the hypopharynx as a complication of anti-TNF therapy. Am J Otolaryngol 2013; 34: 268-272.

[35] Miscia S, Marchisio M, Grilli A, Di Valerio V, Centurione L, Sabatino G, Garaci F, Zauli G, Bonvini E and Di Baldassarre A. Tumor necrosis factor alpha (TNF-alpha) activates Jak1/Stat3-Stat5B signaling through TNFR-1 in human B cells. Cell Growth Differ 2002; 13: 13-18.

[36] Mortaz E, Sereshki HA, Abedini A, Kiani A, Mirsaeidi M, Soroush D, Garssen J, Velayati A, Redegeld FA and Adcock IM. Association of serum TNF-alpha, IL-8 and free light chain with HLA-DR B alleles expression in pulmonary and extra-pulmonary sarcoidosis. J Inflamm (Lond) 2015; 12: 21.

[37] Roach DR, Bean AG, Demangel C, France MP, Briscoe H and Britton WJ. TNF regulates chemokine induction essential for cell recruitment, granuloma formation, and clearance of mycobacterial infection. J Immunol 2002; 168: 4620-4627.

[38] Zhou T, Casanova N, Pouladi N, Wang T, Lussier Y, Knox KS and Garcia JGN. Identification of Jak-STAT signaling involvement in sarcoidosis severity via a novel microRNA-regulated peripheral blood mononuclear cell gene signature. Sci Rep 2017; 7: 4237.

[39] Noor A and Knox KS. Immunopathogenesis of sarcoidosis. Clin Dermatol 2007; 25: 250-258.

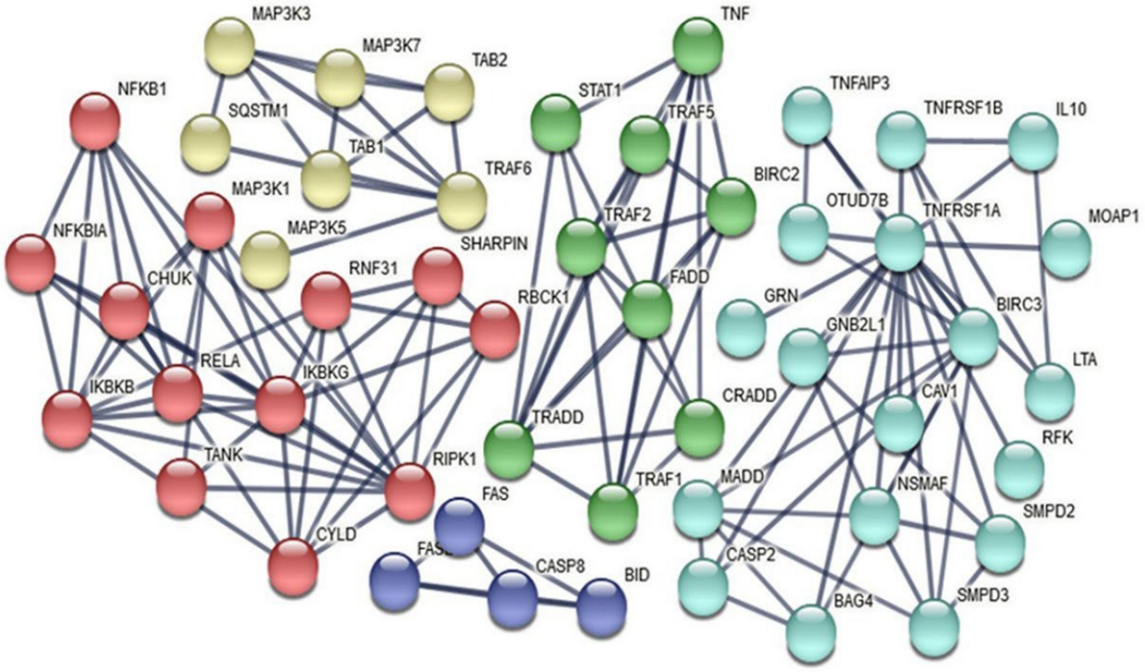

Supplementary Figure 1. Protein-protein interaction network showing subset of the STRING clusters showing with TNF-related proteins association with NHK B, MAP and IL-10 in MWCTN model. Proteins were ranked at the highest confidence (0.9) interaction score, the network edges indicate the confidence, the Kmeans clustering was calculated and subset of five clusters were selected for visualization.

Supplementary Table 1. STRING clusters

term ID	term description	observed gene count	background gene count	strength	false discovery rate	matching proteins in your network (labels)
CL:4847	Mitotic Spindle Checkpoint, and mitotic nuclear division	31	153	0.87	1.01E-13	FAM64A, NCAPG, KIF11, POLQ, C1orf112, BUB1B, CCNB2, MIS18A, MELK, KIAA0101, BIRC5, AURKB,CDCA2, UBE2C, KIF14, ASPM, MKI67, CEP55, KIF2C, PRC1, KIF20A, KIF4B, KIFC1, TOP2A, DEPDC1, HJURP, GTSE1, CDK18, PBK, SPC24, KIF18B
CL:4854	Mixed, incl. condensed chromosome, centromeric region, and kinesin motor, catalytic domain. atpase	28	102	1	2.92E-14	FAM64A, NCAPG, KIF11, POLQ, BUB1B, CCNB2, MIS18A, MELK, KIAA0101, BIRC5, AURKB, CDCA2, UBE2C, KIF14, ASPM, MKI67, CEP55, KIF2C, PRC1, KIF20A, KIF4B, KIFC1, TOP2A, DEPDC1, HJURP, PBK, SPC24, KIF18B
CL:4856	Mixed, incl. mitotic sister chromatid segregation, and gastric cancer network 1	24	68	1.11	2.92E-14	FAM64A, NCAPG, KIF11, BUB1B, CCNB2, MELK, KIAA0101, BIRC5, AURKB, CDCA2, UBE2C, KIF14, ASPM, MKI67, CEP55, KIF2C, PRC1, KIF20A, KIF4B, KIFC1, TOP2A, DEPDC1, PBK, KIF18B
CL:4860	Mixed, incl. mitotic sister chromatid segregation, and gastric cancer network 1	22	58	1.14	6.43E-14	FAM64A, NCAPG, KIF11, BUB1B, CCNB2, MELK, KIAA0101, BIRC5, AURKB, UBE2C, ASPM, MKI67, CEP55, KIF2C, PRC1, KIF20A, KIF4B, KIFC1, TOP2A, DEPDC1, PBK, KIF18B
CL:4861	Mitotic nuclear division, and gastric cancer network 1	21	50	1.19	6.43E-14	FAM64A, KIF11, BUB1B, CCNB2, MELK, KIAA0101, BIRC5, AURKB, UBE2C, ASPM, MKI67, CEP55, KIF2C, PRC1, KIF20A, KIF4B, KIFC1, TOP2A, DEPDC1, PBK, KIF18B
CL:4863	Mixed, incl. mitotic cytokinesis, and gastric cancer network 1	17	45	1.14	1.37E-10	KIF11, BUB1B, CCNB2, MELK, KIAA0101, BIRC5, AURKB, UBE2C, ASPM, MKI67, CEP55, KIF2C, PRC1, KIF20A, TOP2A, DEPDC1, PBK
CL:19706	Mixed, incl. complement and coagulation cascades, and lipoprotein particle	17	182	0.54	5.50E-03	PROCR, FCGRT, C8G, RBMS2, F13A1, C2, C3AR1, C1QB, CLU, CFD, C1QC, C1QA, VSIG4, APOM, THBD, C4B, APOC4
CL:4867	Mixed, incl. mitotic cytokinesis, and gastric cancer network 1	16	39	1.18	2.27E-10	KIF11, BUB1B, CCNB2, MELK, KIAA0101, BIRC5, AURKB, UBE2C, ASPM, MKI67, CEP55, KIF2C, PRC1, KIF20A, TOP2A, PBK
CL:16429	Collagen formation, and Defective B3GALTL causes Peters-plus syndrome (PpS)	16	168	0.54	6.90E-03	SPARC, THSD1, THBS1, NID1, VCAN, COL6A2, COL27A1, COL6A1, THBS2, COL9A2, LOXL2, COL23A1, FBLN2, CD36, SERPINB2, FBN2
CL:4869	Mixed, incl. spindle midzone assembly, and gastric cancer network 1	15	34	1.21	4.83E-10	KIF11, BUB1B, CCNB2, KIAA0101, BIRC5, AURKB, UBE2C, ASPM, MKI67, CEP55, KIF2C, PRC1, KIF20A, TOP2A, PBK
CL:18264	Chemokine receptors bind chemokines, and Intercrine alpha family (small cytokine C-X-C) (chemokine CXC)	13	93	0.71	1.30E-03	ACKR3, CSF1R, CXCL3, CXCL5, CXCL10, CXCL11, CSF1, CCR10, WLS, CXCL9, CCL8, CCL18, CCL3L3
CL:18487	Mixed, incl. nf-kappa b signaling pathway, and card domain	13	126	0.58	1.45E-02	TNFRSF1A, MEFV, CD180, TLR2, USP2, CD14, NLRP3, TNFSF13, TLR4, LY86, NAIP, TLR5, TNFSF14
CL:16430	Collagen formation, and Matrix metalloproteinases	12	129	0.53	4.31E-02	SPARC, NID1, VCAN, COL6A2, COL27A1, COL6A1, COL9A2, LOXL2, COL23A1, FBLN2, SERPINB2, FBN2
CL:4870	Mixed, incl. g^2/m dna replication checkpoint, and gastric cancer network 1	10	22	1.22	2.11E-06	KIF11, BUB1B, CCNB2, KIAA0101, UBE2C, ASPM, MKI67, CEP55, TOP2A, PBK
CL:19966	Complement cascade	10	49	0.87	9.40E-04	C8G, RBMS2, C2, C3AR1, C1QB, CFD, C1QC, C1QA, VSIG4, C4B
CL:18266	Chemokine receptors bind chemokines, and macrophage proliferation	10	67	0.74	7.00E-03	CSF1R, CXCL3, CXCL5, CXCL10, CXCL11, CSF1, CCR10, CXCL9, CCL8, CCL3L3
CL:18491	NF-kappa B signaling pathway, and TIR domain	10	80	0.66	1.81E-02	TNFRSF1A, CD180, TLR2, USP2, CD14, TNFSF13, TLR4, LY86, TLR5, TNFSF14
CL:23089	Voltage-gated potassium channel complex, and interaction between I1 and ankyrins	10	91	0.61	4.08E-02	KCNQ1, KCNJ2, KCNQ4, KCNH4, KCNMB1, KCNF1, KCNE1, MTSS1L, ANK2, SCN1B

CL:16193	Axon guidance, and dendrite self-avoidance	10	92	0.6	4.31E-02	LRRC4, SEMA7A, SEMA3A, NRP1, UNC5A, GPR125, SEMA4A, EPHB2, EFNA4, SRGAP2
CL:19968	Complement cascade	9	37	0.95	9.00E-04	RBMS2, C2, C3AR1, C1QB, CFD, C1QC, C1QA, VSIG4, C4B
CL:19544	Mixed, incl. lrrc8, pannexin-like tm region, and apoptotic cell clearance	9	43	0.89	1.90E-03	ITIH4, MERTK, CD209, OLFML3, BAIAP3, GAS6, GPR34, CLMP, MRC1
CL:18850	Mixed, incl. immunoregulatory interactions between a lymphoid and a non-lymphoid cell, and aig1-type guanine nucleotide-binding (g) domain	9	61	0.73	1.47E-02	LILRA2, FCGR2A, CD300A, MPEG1, FCGR3A, TLR7, LILRB2, LILRB5, GIMAP5
CL:19545	Mixed, incl. apoptotic cell clearance, and ebola hemorrhagic fever	8	29	1.01	1.30E-03	ITIH4, MERTK, CD209, OLFML3, BAIAP3, GAS6, GPR34, CLMP
CL:18851	Mixed, incl. immunoregulatory interactions between a lymphoid and a non-lymphoid cell, and pattern recognition receptor activity	8	47	0.8	1.47E-02	LILRA2, FCGR2A, CD300A, MPEG1, FCGR3A, TLR7, LILRB2, LILRB5
CL:18267	Chemokine receptors bind chemokines	8	60	0.69	4.59E-02	CXCL3, CXCL5, CXCL10, CXCL11, CCR10, CXCL9, CCL8, CCL3L3
CL:19970	Initial triggering of complement, and Complement component 3 deficiency	7	21	1.09	1.60E-03	C2, C3AR1, C1QB, C1QC, C1QA, VSIG4, C4B
CL:19546	Mixed, incl. apoptotic cell clearance, and tmem119 family	6	19	1.06	7.10E-03	MERTK, OLFML3, BAIAP3, GAS6, GPR34, CLMP
CL:18573	IRAK4 deficiency (TLR2/4), and interleukin-1 receptor binding	6	23	0.98	1.47E-02	CD180, TLR2, CD14, TLR4, LY86, TLR5
CL:18276	Chemokine receptors bind chemokines	6	28	0.9	2.89E-02	CXCL3, CXCL5, CXCL10, CXCL11, CXCL9, CCL3L3
CL:4873	Mixed, incl. mitotic chromosome movement towards spindle pole, and stromme syndrome	5	10	1.26	6.70E-03	KIF11, BUB1B, ASPM, MKI67, CEP55
CL:4913	Spindle midzone assembly, and chromosome passenger complex	5	12	1.18	1.07E-02	BIRC5, AURKB, KIF2C, PRC1, KIF20A
CL:19972	Initial triggering of complement	5	16	1.06	2.32E-02	C2, C1QB, C1QC, C1QA, C4B
CL:18607	Lipopolysaccharid e receptor complex, and toxic pneumonitis	4	6	1.39	1.47E-02	CD180, CD14, TLR4, LY86
CL:4914	Chromosome passenger complex, and kinesin-like protein kif20a	4	6	1.39	1.47E-02	BIRC5, AURKB, KIF2C, KIF20A

The gene coding-protein and their associated structural and biological interactors were visualized as hierarchical clusters of the full STRING network by using an average linkage algorithm of publicly available for protein-protein interactions (KEGG, Reactome, BioCyc, and Gene Ontology). Highlighting clusters associated to NF-kappa-B signaling, collagen formation, matrix metalloproteinases and chemokine other inflammatory related terms.

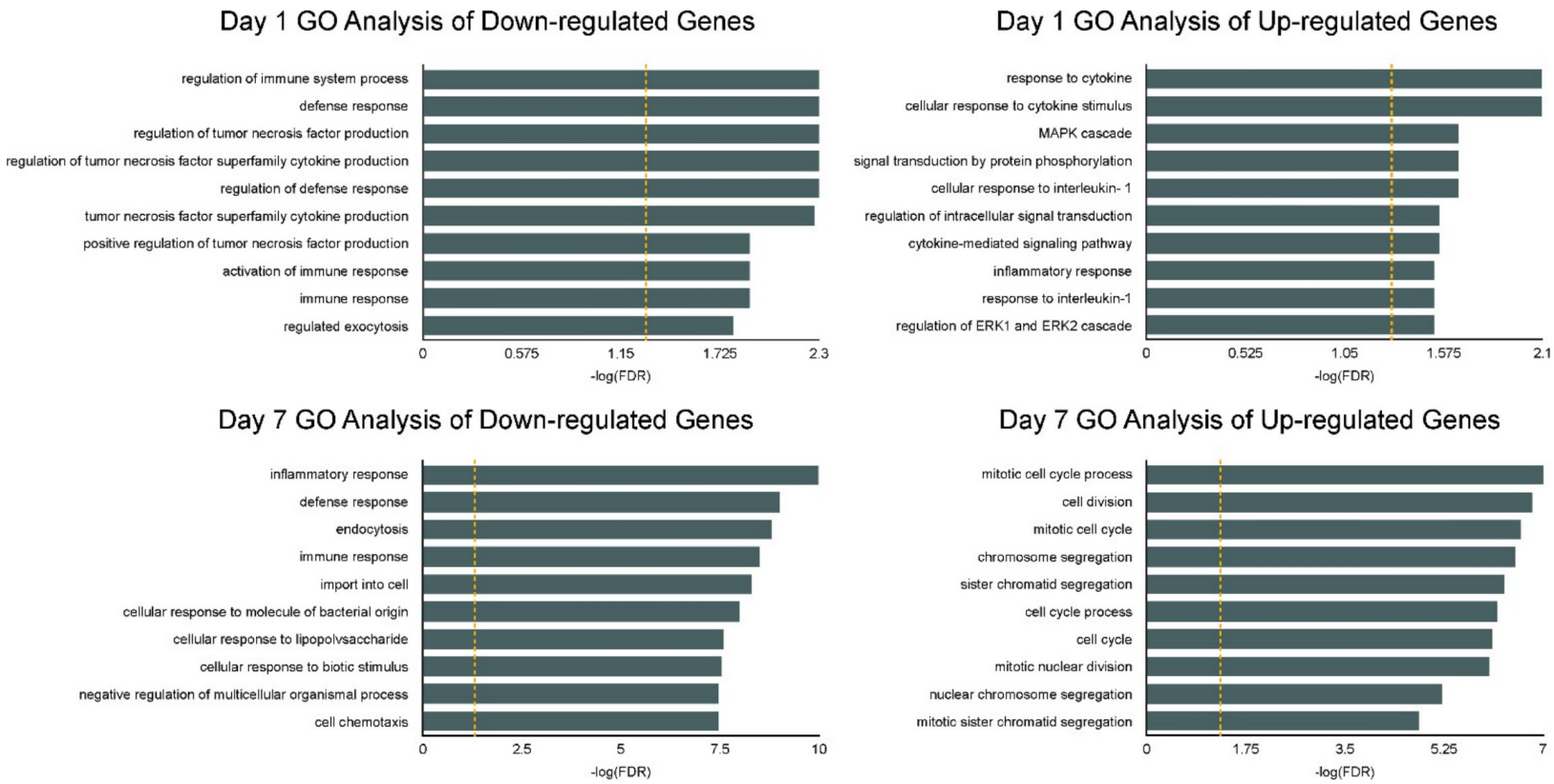

Supplementary Figure 2. The top associated Gene Ontology terms of the DEGs at Day 1 and D7 in the upregulated and downregulated genes.